Supplementary Materials

Binder-free, multidentate bonding-induced carbon nano-oligomer assembly for boosting charge transfer and capacitance of energy nanoparticle-based textile pseudocapacitors

Experimental Section

Synthesis of OA-MnO_x NPs: OA-MnO_x NPs with an average diameter of ~10 nm were synthesized following a previously reported method [S1]. Briefly, 40 mmol of manganese(II) chloride tetrahydrate ($MnCl_2 \cdot 4H_2O$; Sigma-Aldrich) and 80 mmol of sodium oleate (TCI Co. Ltd) were mixed in a solution containing ethanol (30 mL), deionized water (40 mL), and *n*-hexane (70 mL). This mixture was then stirred at 70 ℃ for 12 h. After the completion of reaction, the organic phase was separated from the aqueous phase, washed with deionized water, and evaporated to obtain a pink-colored Mn-oleated complex powder. Subsequently, 1.24 g of Mn-oleated complex was dissolved in 1-hexadecene (12.8 mL; Alfa Aesar) and stirred at 70 ℃ for 1 h under an Ar atmosphere. The reaction mixture was then heated up to 280 ℃ with a constant heating rate of 1.9 ℃ min^{-1} and kept at that temperature for 10 min. The resultant solution was cooled to room temperature and purified through several times of centrifugation with excess acetone and ethanol. The obtained OA-MnO_x NPs were dispersed in toluene for futher use.

Synthesis of CNOs: 0.5 g of pristine carbon blacks (EQ-Lib-Super P; MTI Korea) underwent surface treatment in a mixture of H_2SO_4 (30 mL, 98%) and HNO_3 (10 mL, 60%) at 70 ℃ for 3 h with stirring. After the reaction, the resultant solution was cooled to room temperature and slowly neutralized by adding deionized water. Then, the CNOs were separated through centrifugation and subjected to vacuum filtration to remove residual acid. The filtrated CNO films were dried in a vacuum oven and dispersed in ethanol for further use.

Synthesis of OA-Fe_3O_4 NPs: OA-Fe_3O_4 NPs with an average diameter of ~10 nm were synthesized by referring to a previously reported method [S2], and all chemicals were purchased from Sigma-Aldrich. Briefly, a mixture of iron(III) acetylacetonate ($Fe(acac)_3$, 2.0 mmol), 1,2-hexadecandiol (10 mmol), oleic acid (OA, 6.0 mmol), oleylamine (OAm, 6.0

mmol), and benzyl ether (20 mL) was stirred under an Ar atmosphere. Subsequently, the mixture solution was heated at 200 ℃ for 2 h and then at 300 ℃ for 1 h. After cooling the resultant solution to room temperature, centrifugation with excess acetone and ethanol was repeated to precipate the OA-Fe_3O_4 NPs. These precipitants were redissolved in toluene containing OA (0.05 mL) and OAm (0.05 mL). After several additional centrifugation processes, the final OA-Fe_3O_4 NPs were dipsersed in toluene for furher use.

Preparation of NTCs: First, bare cotton textiles was thoroughly cleaned with deionized water and dried in a vacuum oven at room temperature. Under a continuous N_2 gas flow, they were carbonized by heating up to 950 ℃ at a constant heating rate of 3.0 ℃ min^{-1} and holding for 3 h in a tube furnace, followed by cooling to room temperature. For the Ni electroplating of the carbonized textiles, a Watts bath was prepared by dissolving nickel(II) sulfate hexahydrate ($NiSO_4 \cdot 6H_2O$, 240 g L^{-1}; Alfa Aesar), nickel(II) chloride hexahydrate ($NiCl_2 \cdot 6H_2O$, 45 g L^{-1}; Sigma-Aldrich), and boric acid (H_3BO_3, 30 g L^{-1}; Alfa Aesar) in deionized water [S3]. The carbonized textiles (as a cathode) and high-purity Ni plates (as an anode) were immersed in the Watts bath and electroplating was conducted at a current density of 100 mA cm^{-2} for 20 min using a power supply. The formed NTCs were washed with deionized water and completely dried in a vacuum oven at room temperature.

Direct Multidentate Assembly of (MnO_x or Fe_3O_4 NP/CNO)$_n$ Multilayers: Substrates, including Si wafers, Au-sputtered Si wafers, QCM eletrodes, quartz glasses, ITO glasses, and Ni plates, were irradiated to UV-ozone cleaning for 30 min. In the case of NTCs, they were used without further treatment. After then, all substrates were dipped in a polyethyleneimine (PEI, M_w ~800; Sigma-Aldrich) solution (in ethanol, 5.0 mg mL^{-1}) for 30 min to generate a robust underlayer and rinsed with pure ethanol to remove loosely attached PEI molecules. The PEI-coated substrates were then dipped into a metal oxide NP (MnO_x or Fe_3O_4 NP) solution (in toluene, 10 mg mL^{-1}) for 10 min and rinsed with pure toluene to remove loosely attached

NPs. Subsequently, they were dipped into a CNO solution (in ethanol, 2.0 mg mL^{-1}) for 10 min and rinsed with pure ethanol, resulting in the formation of one bilayer of (MnO_x or Fe_3O_4 NP/CNO) film. These procedures were repeated until the desired bilayer number (*n*) was achieved.

Preparation of (MnO_x slurry)-NTCs: The slurry was prepared by physically blending 80 wt% of MnO_2 powder (average particle size ~10 μm; Sigma-Aldrich), 10 wt% of pristine carbon blacks, and 10 wt% of poly(acrylic acid) (PAA, M_v ~450,000; Sigma-Aldrich) binder in ethanol. The as-prepared slurry was casted on NTCs and then dried in a vacuum oven at 120 °C for 8 h to produce (MnO_x slurry)-NTCs with a MnO_x loading mass of ~5.0 mg cm^{-2}.

Preparation of NTC-AFCs: (MnO_x NP/CNO)-NTCs and (Fe_3O_4 NP/CNO)-NTCs were used as positive and negative electrodes for NTC-AFCs, respectively. The area ratio of the electrodes was precisely controlled based on the following charge balance equations [S4]:

$$q = C \times \Delta E \times m \quad (1)$$

$$\frac{m^+}{m^-} = \frac{C^-\Delta E^-}{C^+\Delta E^+} \quad (2)$$

where *q*, *C*, Δ*E*, and *m* represent the stored charge, areal capacitance (mF cm^{-2}), potential window (V) during CV scans, and area (cm^2) of the positive/negative electrodes, respectively. Based on these equations, the area ratio of positive (MnO_x NP/CNO)-NTCs and negative (Fe_3O_4 NP/CNO)-NTCs was adjusted to 1:1.3.

Characterization: The morphology and crystal structure of the NPs were investigated through HR-TEM (Tecnai 20, FEI). The crystallinity of the NPs was also examined by XRD

using a SmartLab instrument (Rigaku) with Cu K_α radiation (45 kV, 200 mA). The electrical properties of CNOs films on SiO_2/Si wafers were measured with a four-probe method using a Loresta-GP MCP-T610 (Mitsubishi Chemical Analytech). For interfacial chemistry analysis, FTIR spectra was acquired using a Cary 600 (Agilent Technology) with a resolution of 4 cm^{-1}. The obtained FTIR data were baseline-corrected and smoothed through spectrum analysis software (OMNIC, Thermo Fisher Scientific). The contact angles of the multilayers on Si wafers were monitored through a Phoenix-300 instrument (SEO Corp.) using water droplets with a pH of ~5.8. The qualitative growth of the multilayers was investigated through UV-vis spectroscopy (Lambda 365, Perkin Elmer) within the scan range of 800 to 250 nm. The mass change (Δm, μg cm^{-2}) of each layer were quantitively calculated from the frequency change (ΔF, Hz) in QCM measurements (QCM 200, SRS) using a simplified equation derived from the Sauerbrey equation [S5].

$$\Delta F = 56.6 \times \Delta m \quad (3)$$

The film thickness, surface morphology, and EDS images were observed through FE-SEM (S-4800, Hitachi). The current (I)-voltage (V) profiles of the multilayers were measured through a semiconductor parameter analyzer (Agilent 4155B, Agilent Technology) using two gold wires (diameter ~0.5 mm) as the top and bottom electrodes, respectively.

Electrochemical measurements. Electrochemical performance was evaluated through a Ivium-n-Stat workstation (Ivium Technology). For a three-electrode system, Pt mesh and Ag/AgCl (saturated with 3.0 M NaCl) electrode were used as counter and reference electrodes, respectively. For a two-electrode system, the NTC-AFCs (consisiting of (MnO_x NP/CNO)-NTCs as positive electrodes and (Fe_3O_4 NP/CNO)-NTCs as negative electrodes) were evaluated using an aqueous Na_2SO_4 electrolyte (for aqeuous AFCs) and a Na_2SO_4/PVA

gel electrolyte (for solid-state AFCs). In this case, the Na_2SO_4/PVA gel electrolyte was obtained by mixing 1.0 M Na_2SO_4 with polyvinyl alcohol (PVA, 6.0 g) in 60 mL of deionized wtater at 90 ℃ for 1 h. CV and GCD tests were measured in the range of 0 to 0.8 V (for the positive electrodes) and 0 to −0.8 V (for the negative electrodes) *vs.* Ag/AgCl. EIS measurements were carried out in the frequency range of 10^5 to 0.01 Hz with a perturbation amplitude of 0.01 mV. The areal, specific, and volumetric capacitance (*C*) values of electrodes were obtained from GCD curves using the following equation:

$$C = \frac{I\Delta t}{S\Delta V} \quad (4)$$

where *I*, Δ*t*, and Δ*V* are the discharge current density (A), discharge time (s), and operating potential window (V), respectively. The variable (*S*) indicates the active area (cm^2) for the areal capacitance, the active mass (g) for the specific capacitance, or the active volume (cm^3) for the volumteric capacitance of the electrodes. To separate capacitive- (k_1v) and diffusion-controlled ($k_2v^{1/2}$) currents in the scan rate-dependent CV curves, we used the Dunn's method [S6].

$$i(V) = k_{1(V)}v + k_{2(V)}v^{1/2} \quad (5)$$

Here, k_1 and k_2 are constants at a certain potential (*V*). The values of k_1 and k_2 can be obtained by plotting $i(V)/v^{1/2}$ *vs.* $v^{1/2}$, where k_1 and k_2 are the slopes and y-intercepts, respectively. The areal energy density (*E*, mWh cm^{-2}) and power density (*P*, mW cm^{-2}) values of the NTC-AFCs were calculated from GCD curves based on previously defined relationships.

$$E = \frac{CV^2}{7200} \quad (6)$$

$$P = \frac{E \times 3600}{\Delta t} \quad (7)$$

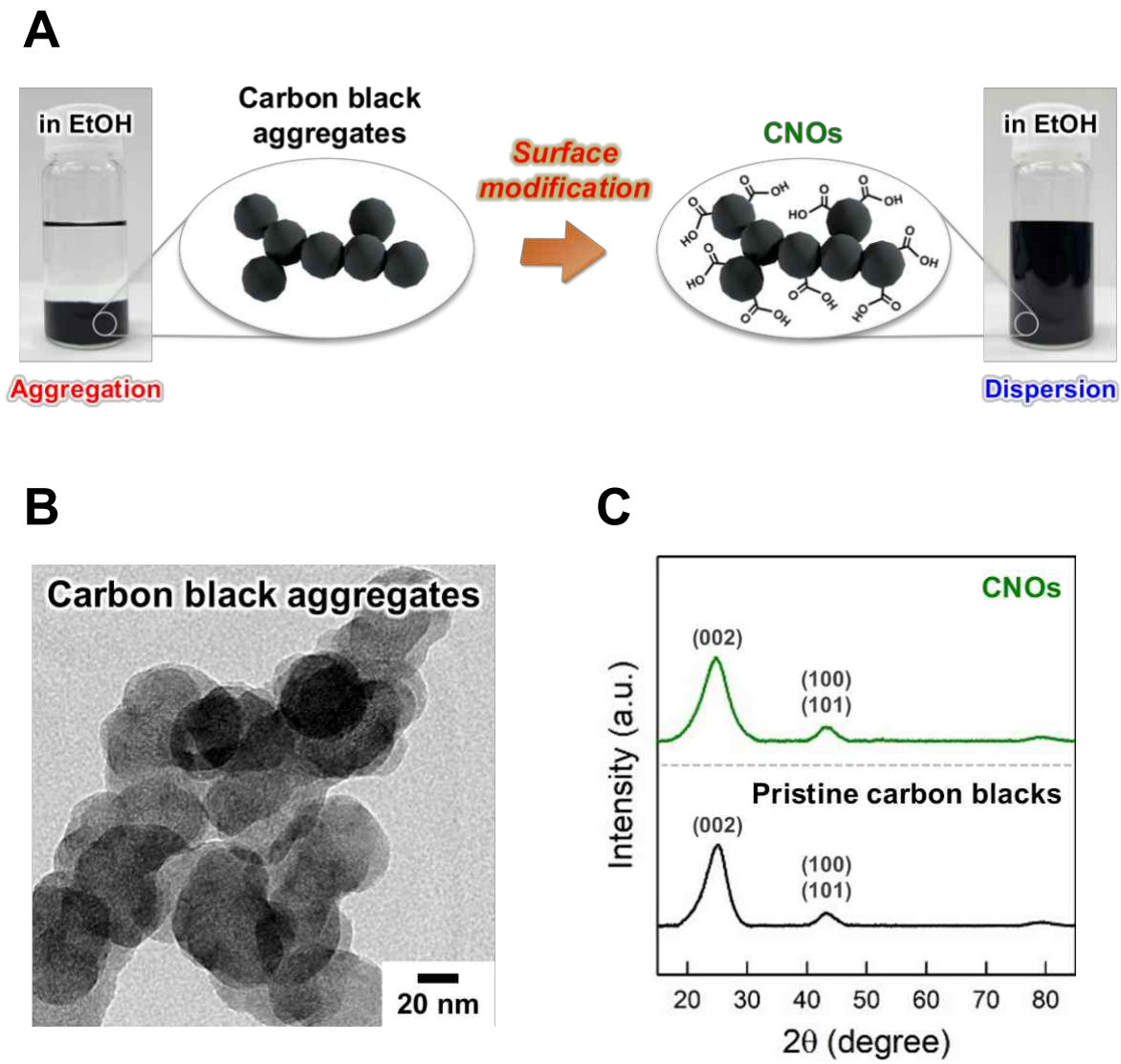

Fig. S1. (A) Schematic illustrations and digital images of pristine carbon black aggregates and CNOs in ethanol. Notably, the pristine carbon blacks were aggregated in ethanol, whereas the surface-modified CNOs exhibited an excellent dispersion stability in the same solvent. (B) HR-TEM image of carbon black aggregates. (C) XRD patterns of CNOs (top) and pristine carbon blacks (bottom).

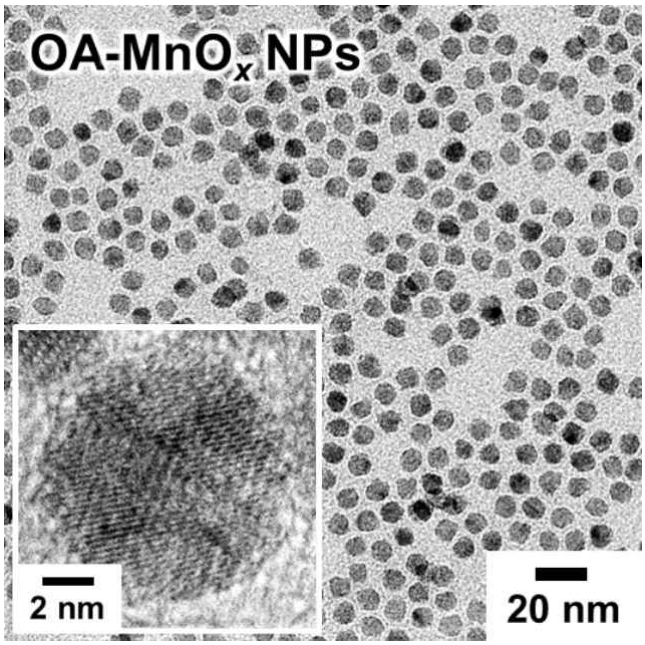

Fig. S2. HR-TEM images of OA-MnO_x NPs with an average diameter of ~10 nm.

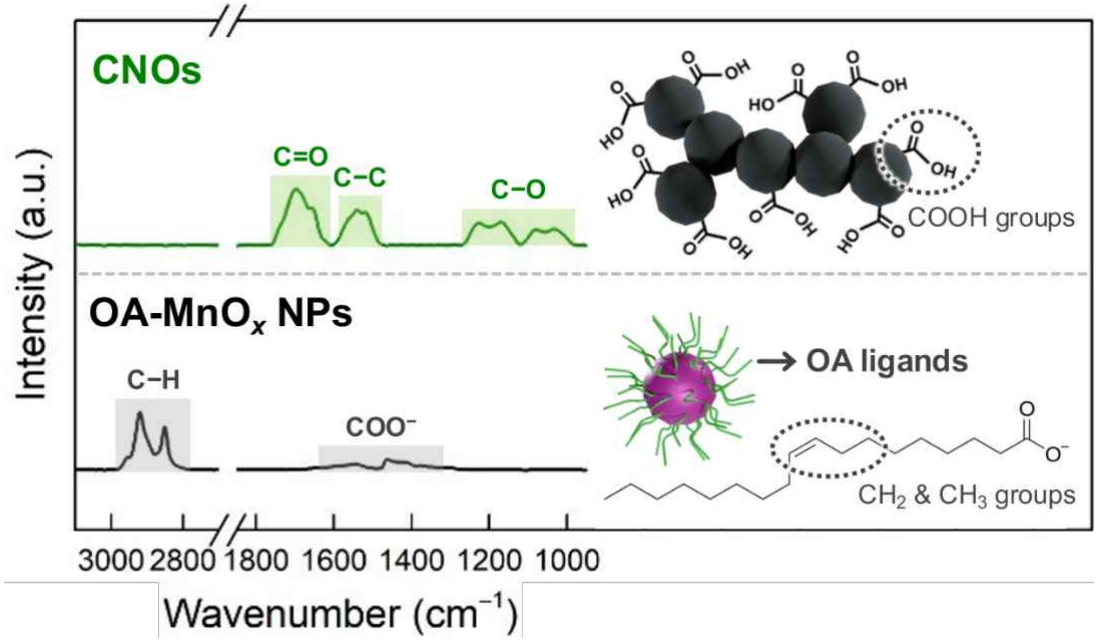

Fig. S3. FTIR spectra of CNOs (top) and OA-MnO_x NPs (bottom). The OA-MnO_x NPs showed distinctive C−H stretching peak (at 3000−2800 cm^{-1}) derived from the long alkyl chains (CH_2 and CH_3 groups) of native OA ligands. On the other hand, the CNOs did not exhibit any notable absorption in the same wavelength region.

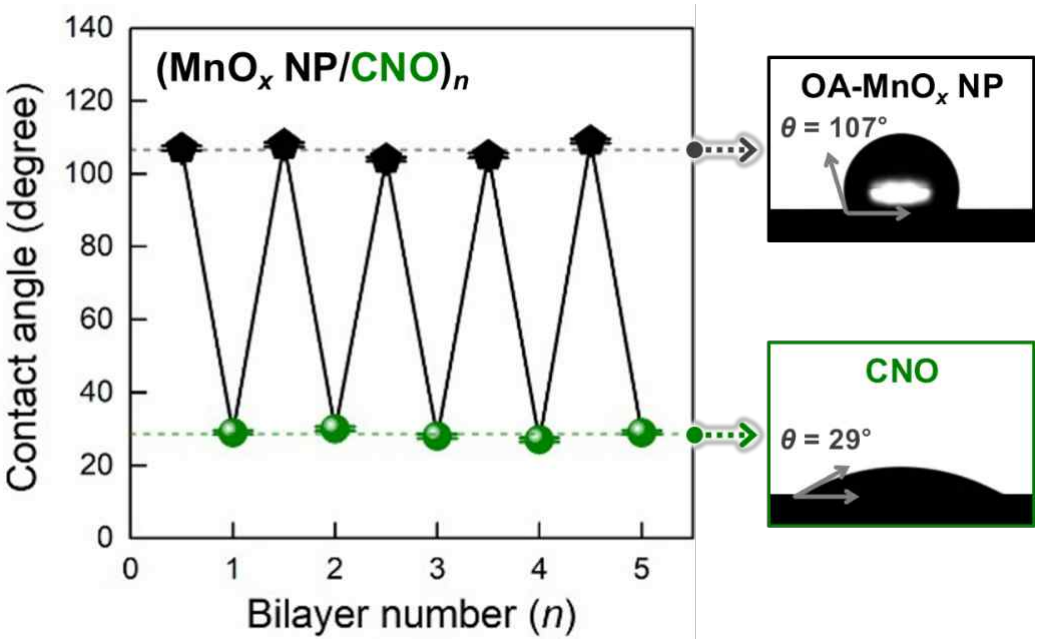

Fig. S4. Water contact angle changes of $(MnO_x$ NP/CNO$)_n$ multilayers as a function of bilayer number (n), along with digital images for the outermost layer of OA-MnO_x NPs (top) and CNOs (bottom). The average water contact angles were measured to be ~107˚ for the outermost layer of OA-MnO_x NPs (n = 0.5, 1.5, 2.5 ...) and ~29˚ for the outermost layer of CNOs (n = 1.0, 2.0, 3.0 ...).

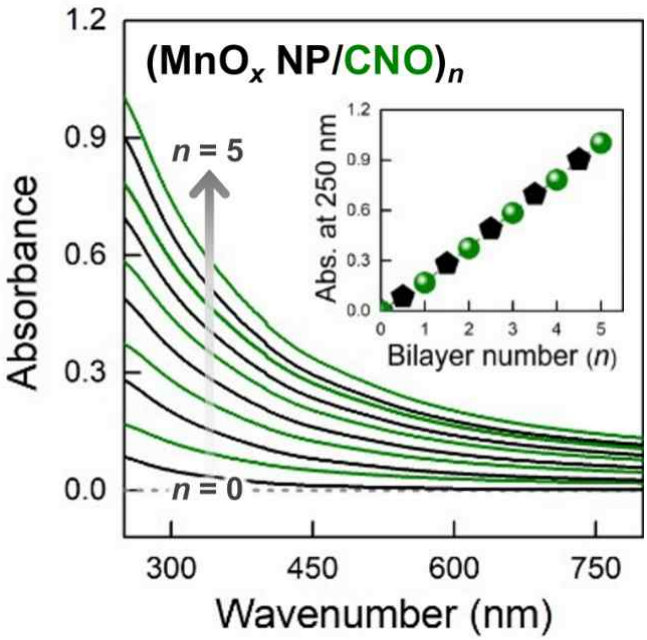

Fig. S5. UV-vis absorbance spectra of $(MnO_x$ NP/CNO$)_n$ multilayers with increasing the bilayer number (n) from 0 to 5 in the wavelength from 800 to 250 nm. The inset represents the absorbance values at the wavelength of 250 nm, indicating a linear growth of the multilayers.

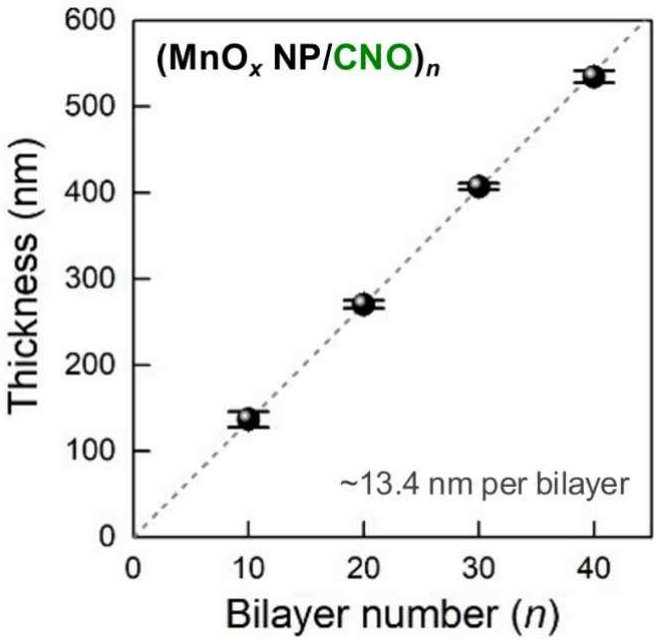

Fig. S6. Film thickness changes of (MnO_x NP/CNO)$_n$ multilayers with increasing the bilayer number (n) increased from 0 to 40 (average film thickness per bilayer ~13.4 nm).

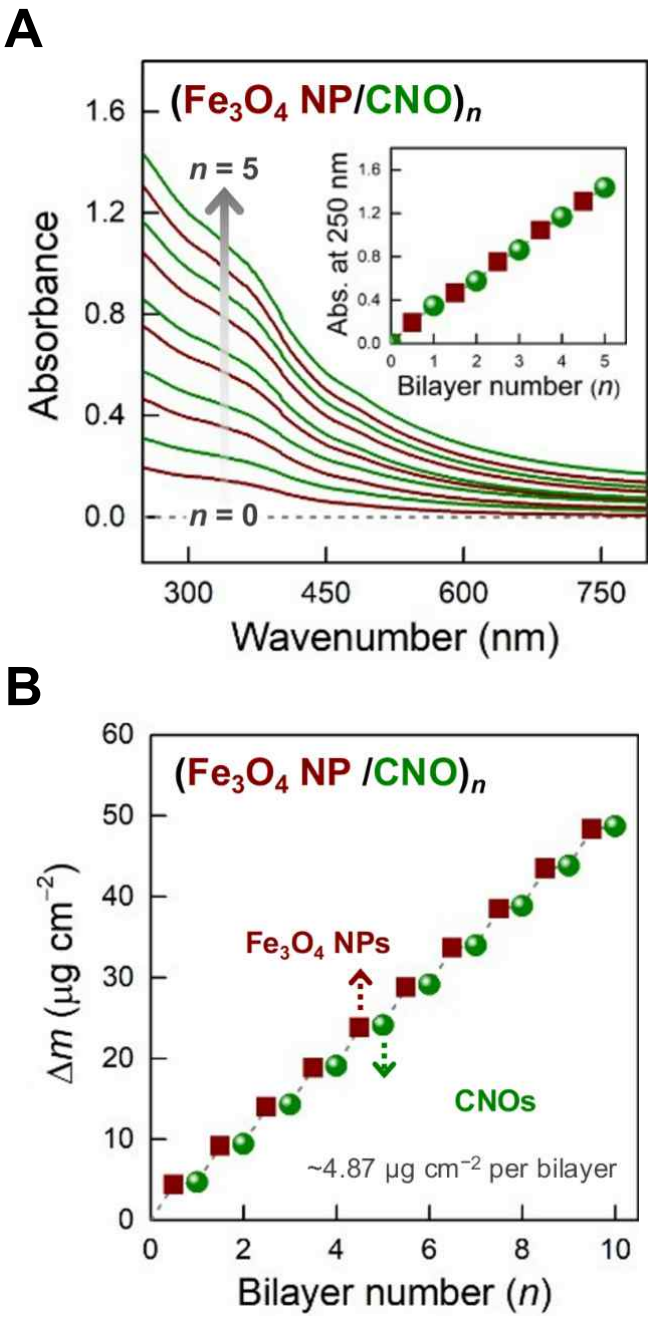

Fig. S7. (A) UV-vis absorbance spectra and (B) mass changes (Δm) (obtained from QCM measurement) of $(Fe_3O_4$ NP/CNO$)_n$ multilayers with increasing the bilayer number (n).

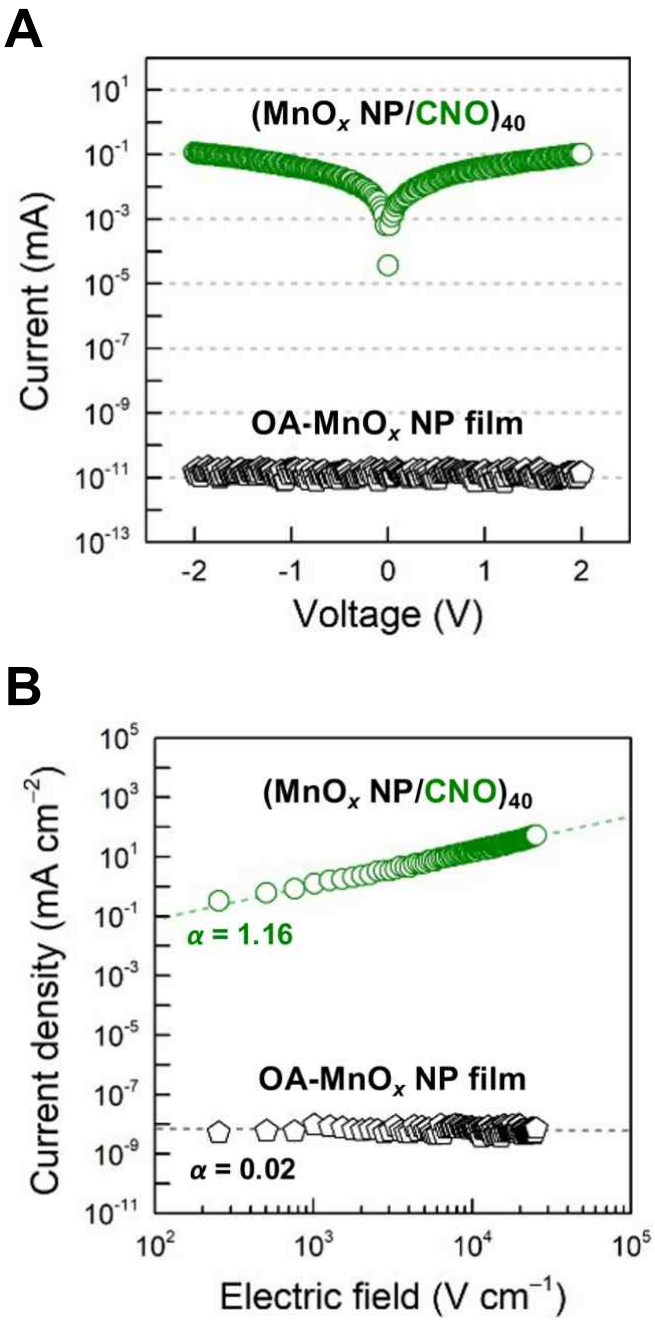

Fig. S8. (A) Current (log *I*) *vs.* voltage (log *V*) and (B) current density (log *J*) *vs.* electric field (log *E*) profiles of $(MnO_x$ NP/CNO$)_{40}$ multilayers and pristine OA-MnO_x NP films.

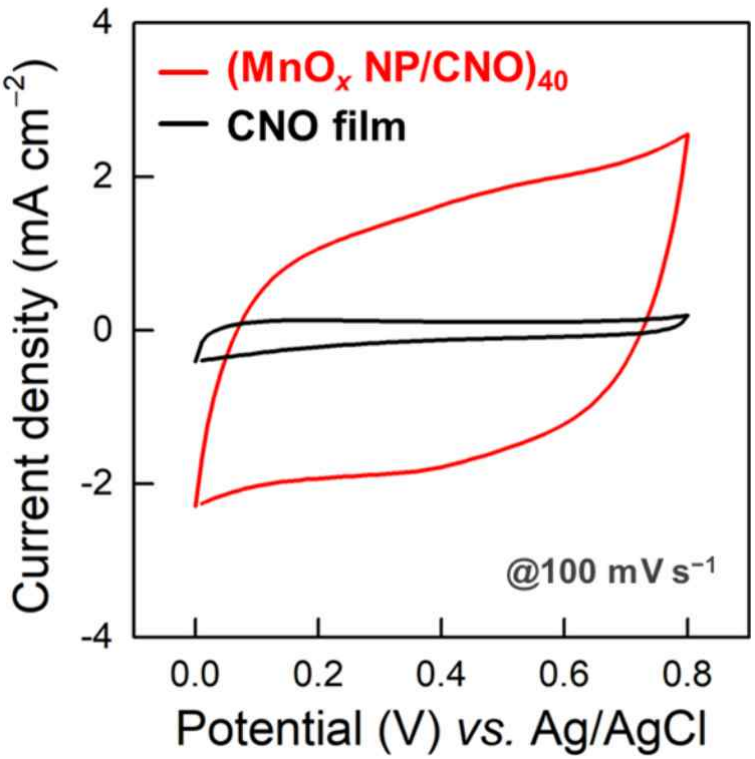

Fig. S9. Comparison of CV curves between $(MnO_x$ NP/CNO$)_{40}$ electrodes and CNO films with the same loading mass of CNOs at 100 mV s^{-1}.

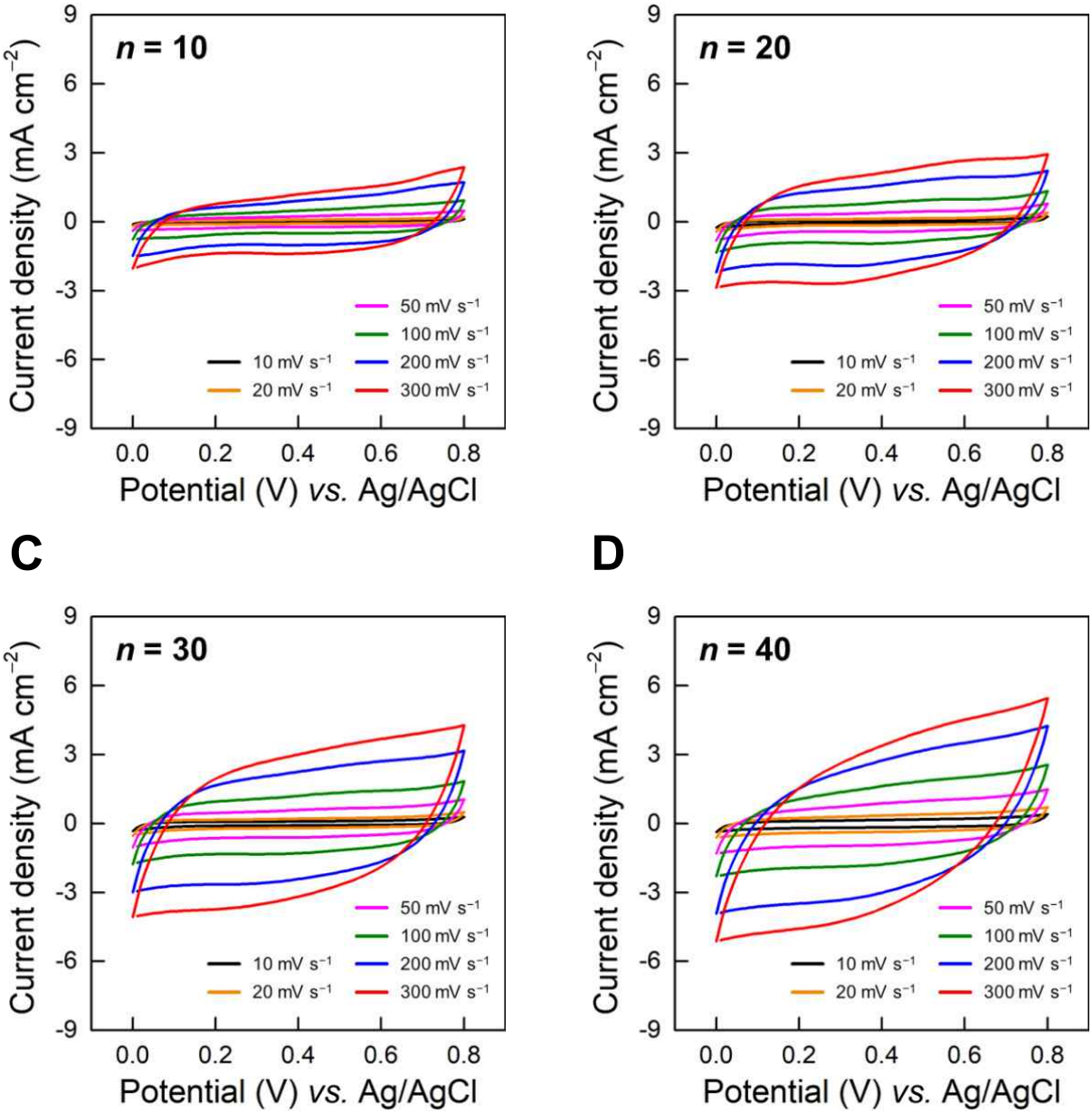

Fig. S10. Scan rate-dependent CV curves of $(MnO_x$ NP/CNO$)_n$ electrodes at different bilayer number (n): (A) n = 10, (B) n = 20, (C) n = 30, and (D) n = 40.

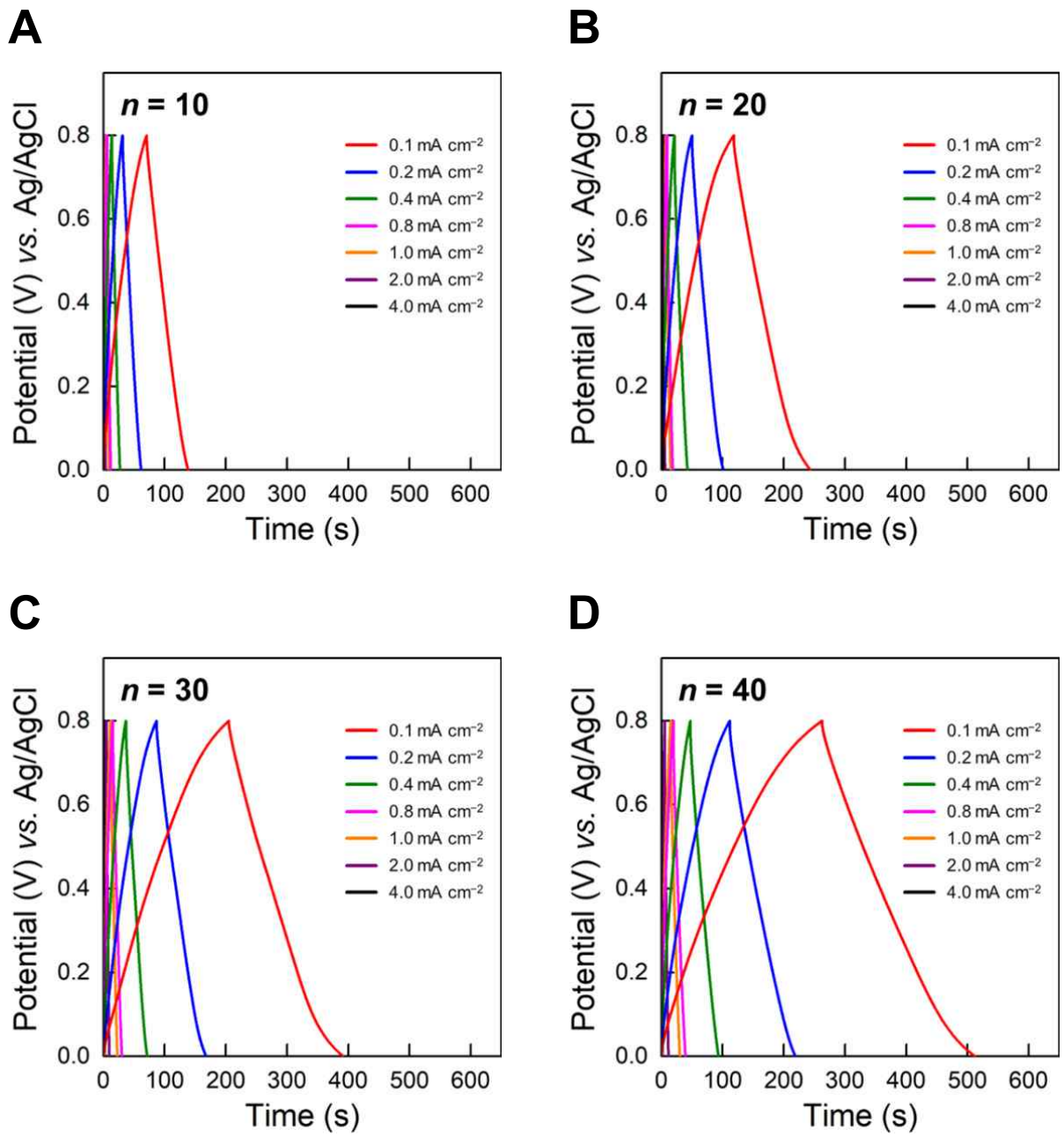

Fig. S11. Current density-dependent GCD curves of $(MnO_x$ NP/CNO$)_n$ electrodes at different bilayer number (n): (A) n = 10, (B) n = 20, (C) n = 30, and (D) n = 40.

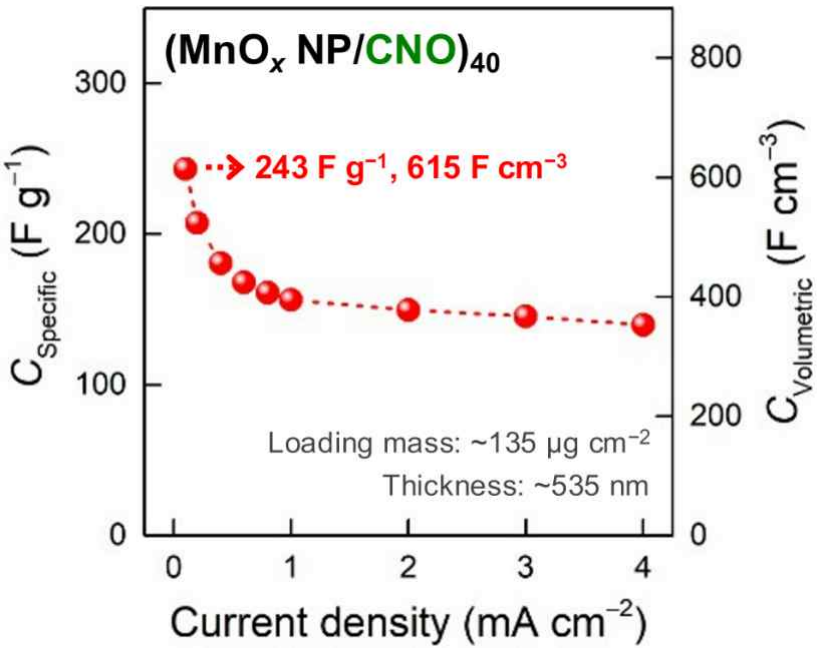

Fig. S12. Specific ($C_{Specific}$, left axis) and volumetric ($C_{Volumetric}$, right axis) capacitance values of $(MnO_x$ NP/CNO$)_{40}$ electrodes at various current densities in the range of 0.1 to 4.0 mA cm^{-2}.

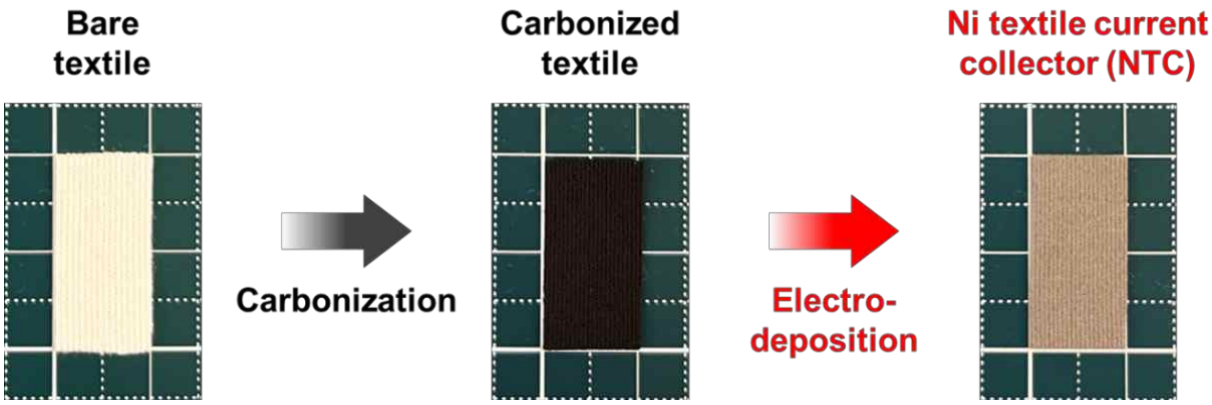

Fig. S13. Procedure of preparing Ni textile current collectors (NTCs) and digital images of each step (see the details in Experimental Section).

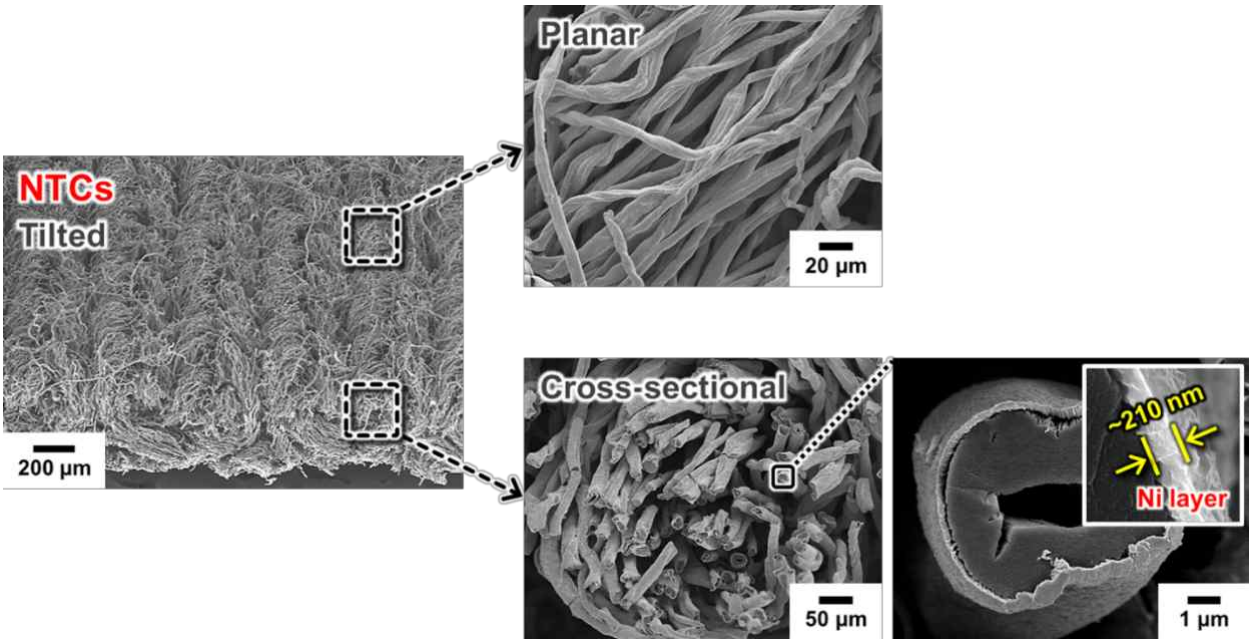

Fig. S14. Tilted, planar, and cross-sectional FE-SEM images of porous NTCs. A thin Ni layer of ~210 nm was uniformly coated all outer/inner fibrils within the NTCs without blocking the pores.

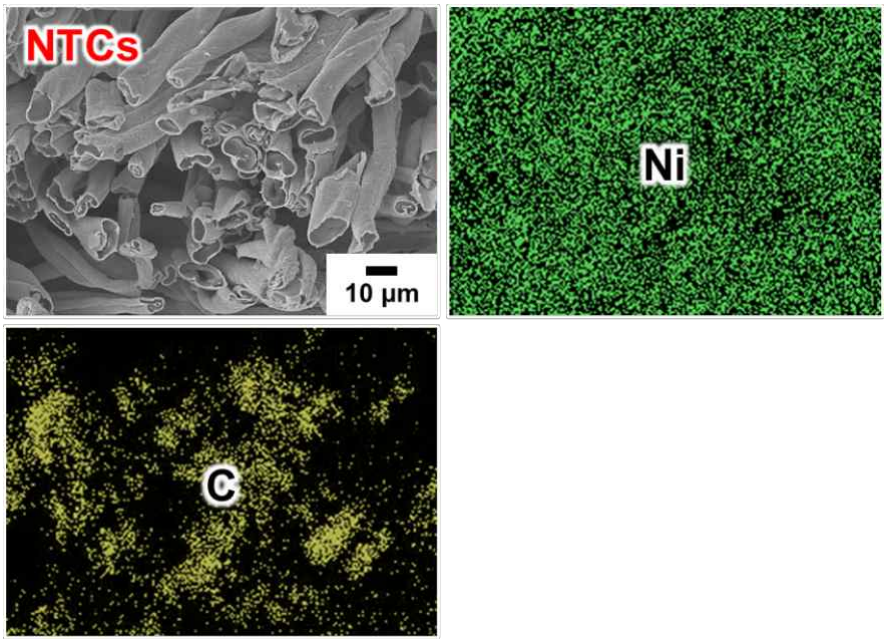

Fig. S15. EDS mapping images of porous NTCs.

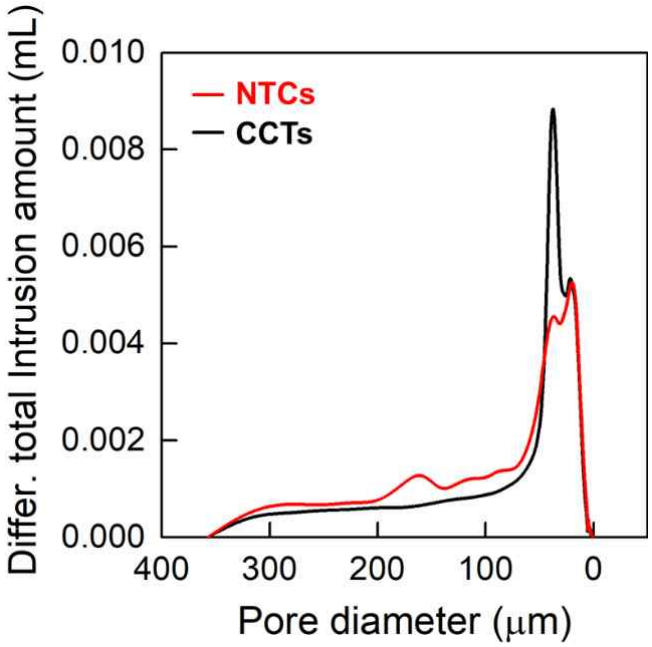

Fig. S16. MIP analysis for CCTs and NTCs. The total surface area of the CCTs was determined to be ~225.2 cm^2 (at an electrode size of 1cm × 2 cm), which was relatively higher than that of the NTCs (~173.3 cm^2). This decrease in surface area of the NTCs was mainly attributed to the overall reduction in pore size within the textiles due to the electrodeposition of the Ni layer.

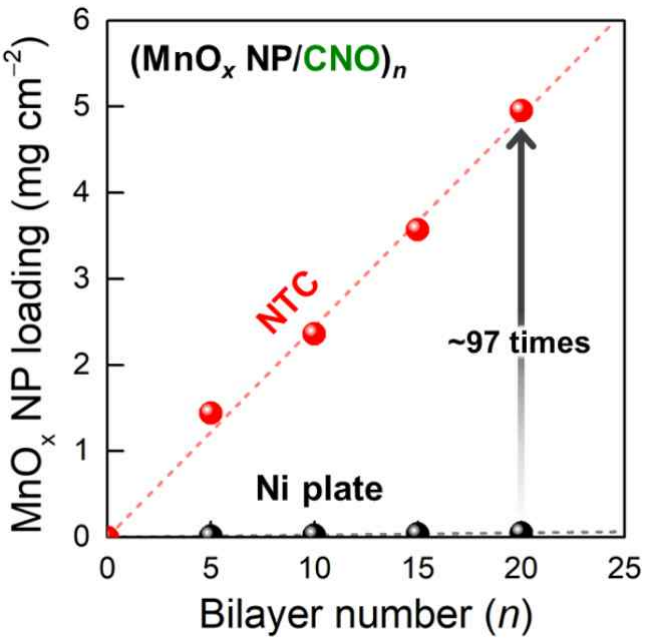

Fig. S17. Loading mass of MnO_x NPs on porous NTCs and flat Ni plates with increasing the bilayer number (n) from 0 to 20.

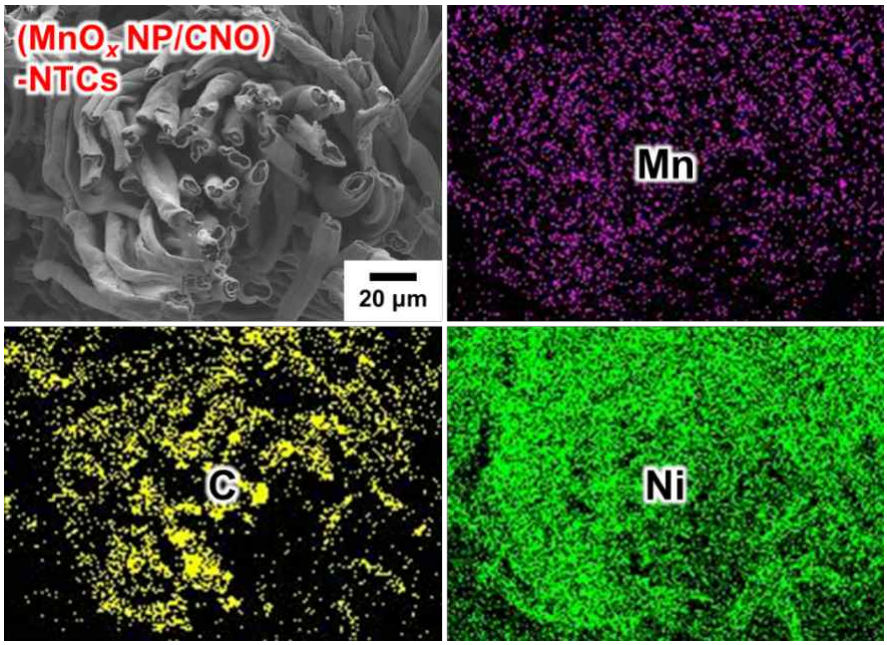

Fig. S18. Cross-sectional FE-SEM and corresponding EDS mapping images of (MnO_x NP/CNO)-NTCs.

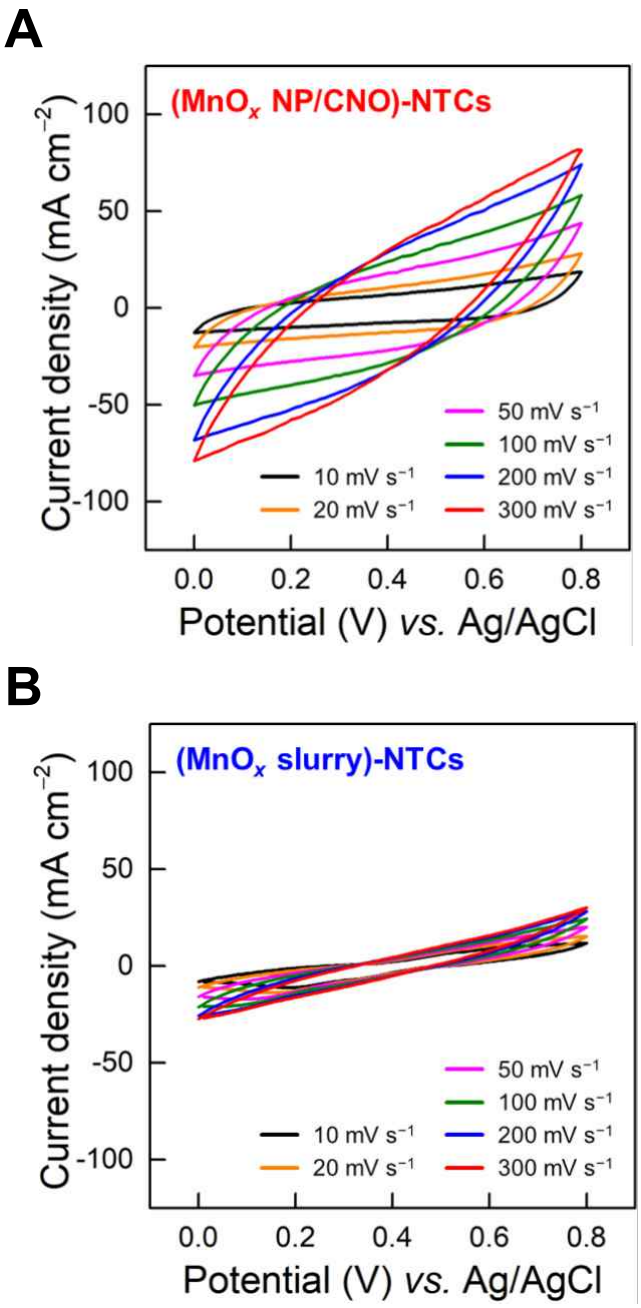

Fig. S19. CV curves of (A) (MnO_x NP/CNO)-NTCs and (B) (MnO_x slurry)-NTCs at various scan rates in the range of 10 to 300 mV s^{-1}.

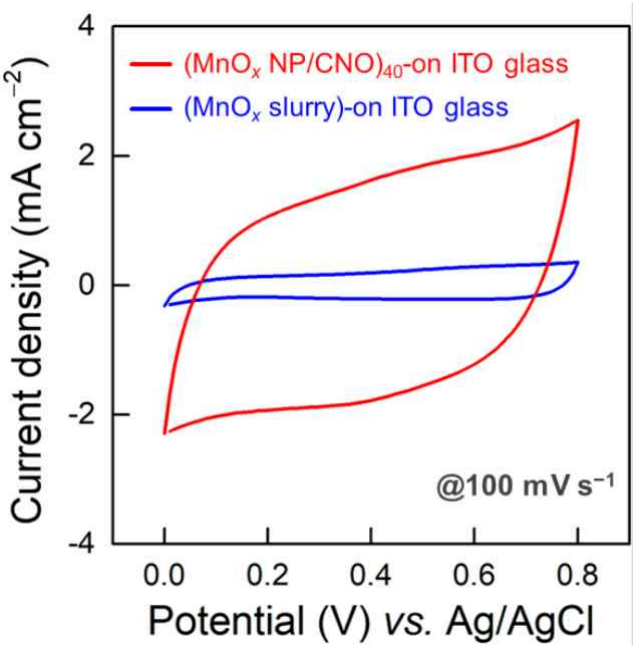

Fig. S20. Comparison of CV curves between the electrode layers of (MnO_x NP/CNO) and (MnO_x slurry) using the 2D flat ITO current collectors at 100 mV s^{-1}.

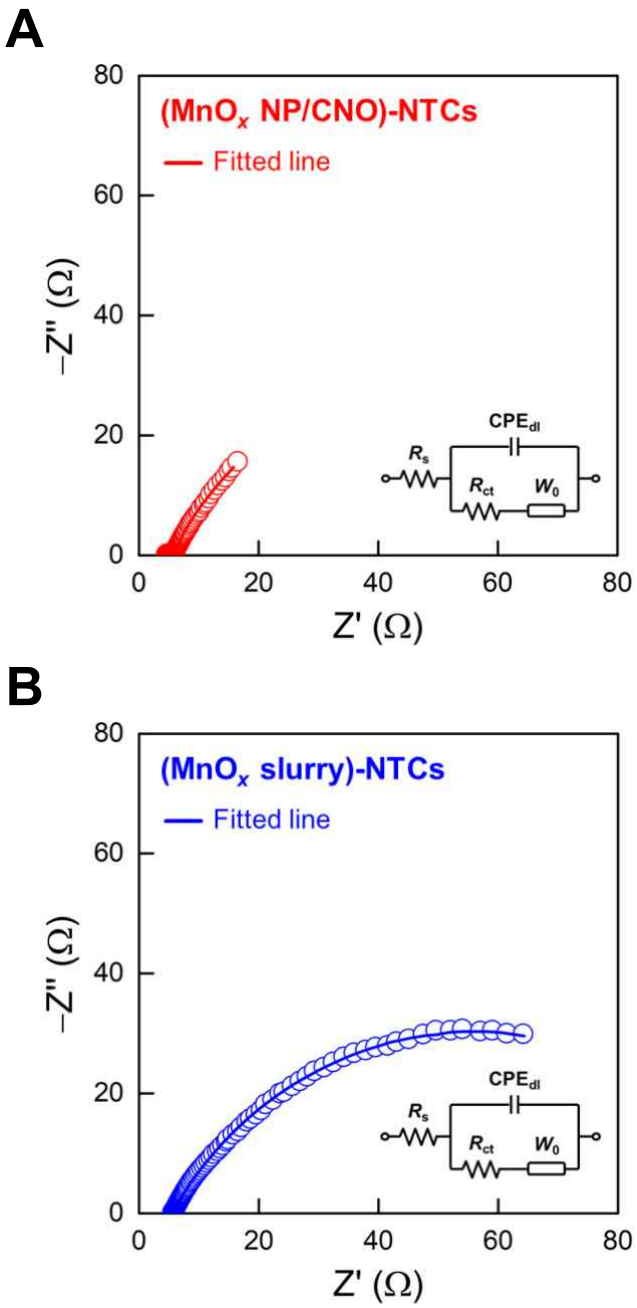

Fig. S21. Nyquist plots and fitted lines using a Randle circuit model (inset) of (A) (MnO_x NP/CNO)-NTCs and (B) (MnO_x slurry)-NTCs.

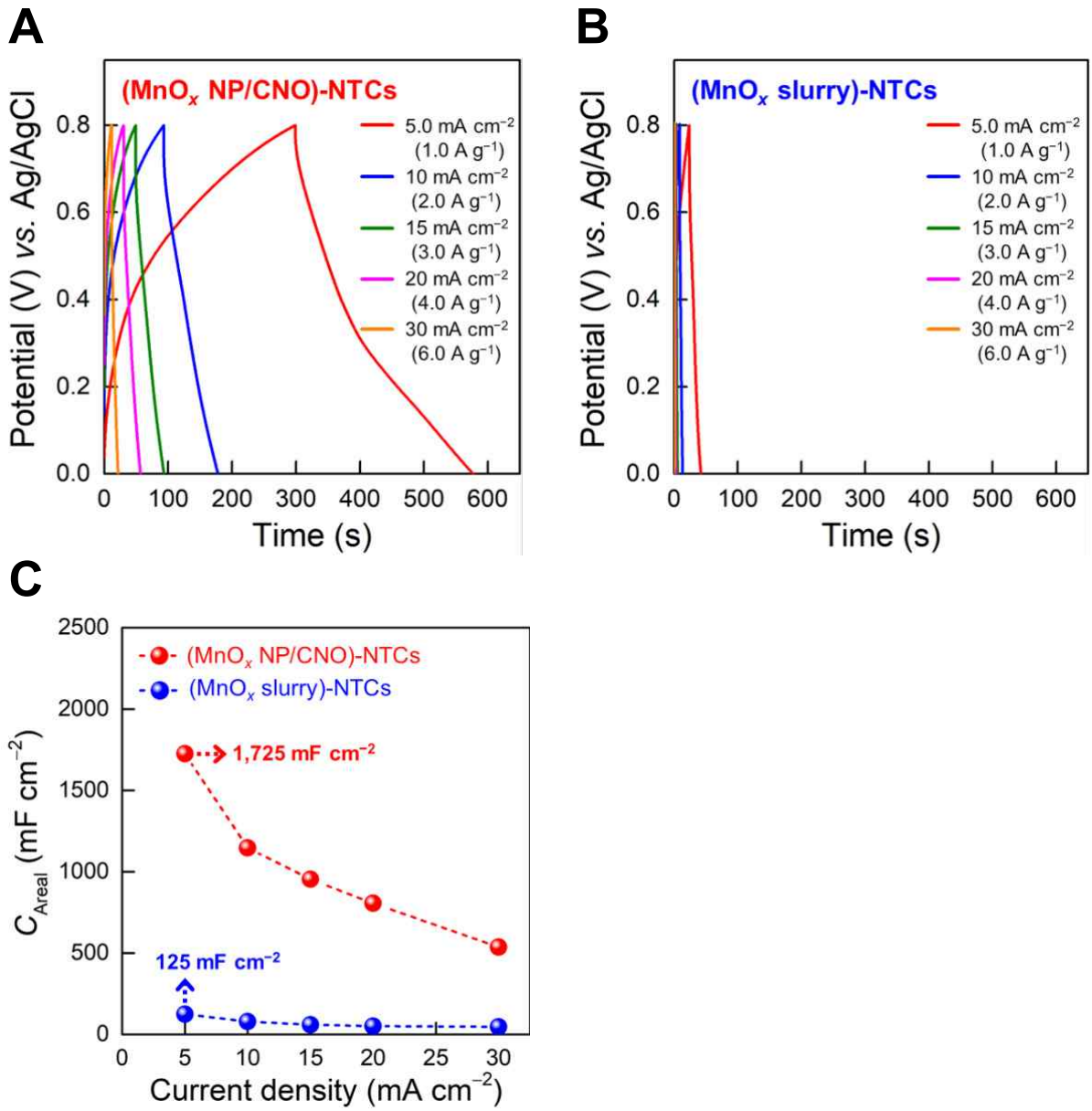

Fig. S22. Current density-dependent GCD curves of (A) (MnO_x NP/CNO)-NTCs and (B) (MnO_x slurry)-NTCs. (C) Areal capacitance (C_{Areal}) values of (MnO_x NP/CNO)-NTCs and (MnO_x slurry)-NTCs at various current densities in the range of 5 to 30 mA cm^{-2}.

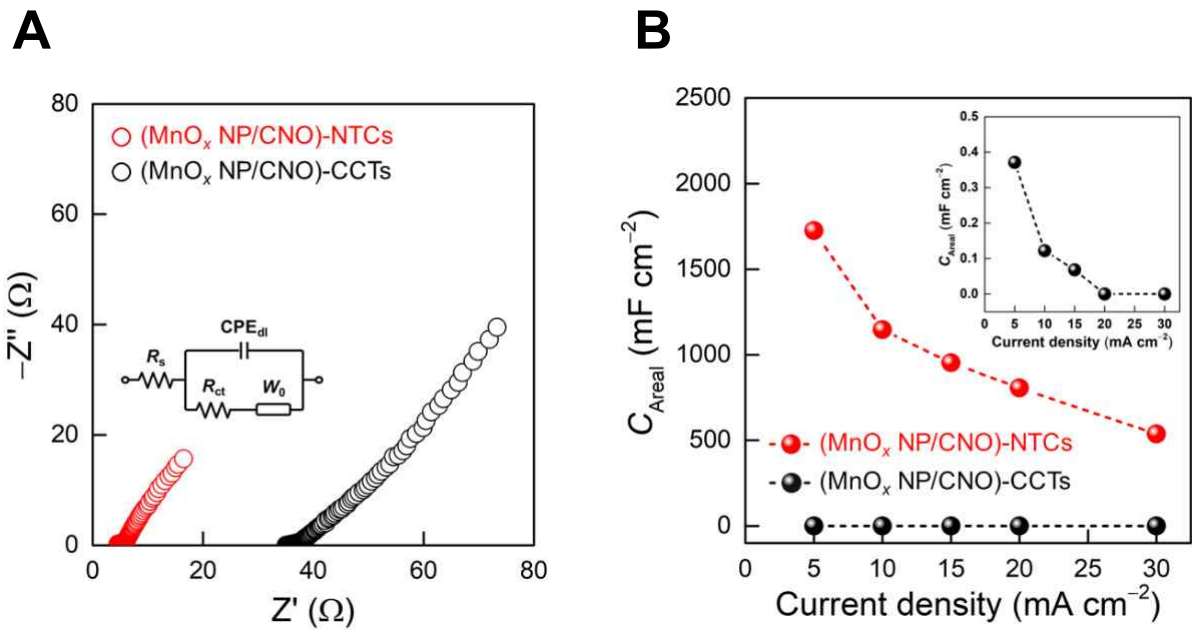

Fig. S23. Comparison of (A) Nyquist plots and (B) areal capacitance (C_{Areal}) values (at different current densities in the range of 1.0 to 6.0 A g^{-1}) between the NTC-based electrodes and the CCT-based electrodes with the same loading mass of electrode layers (*i.e.*, $(MnO_x$ NP/CNO$)_n$ multilayers).

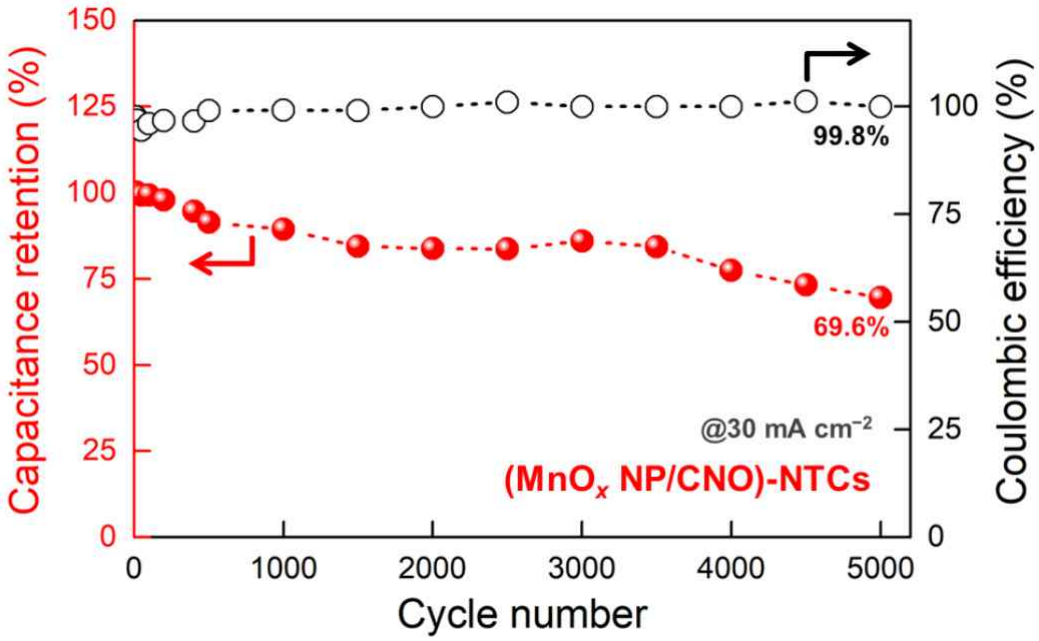

Fig. S24. Cycling stability of (MnO_x NP/CNO)-NTCs, showing a capacitance retention of ~69.6% after GCD 5,000 cycles at 30 mA cm^{-2}.

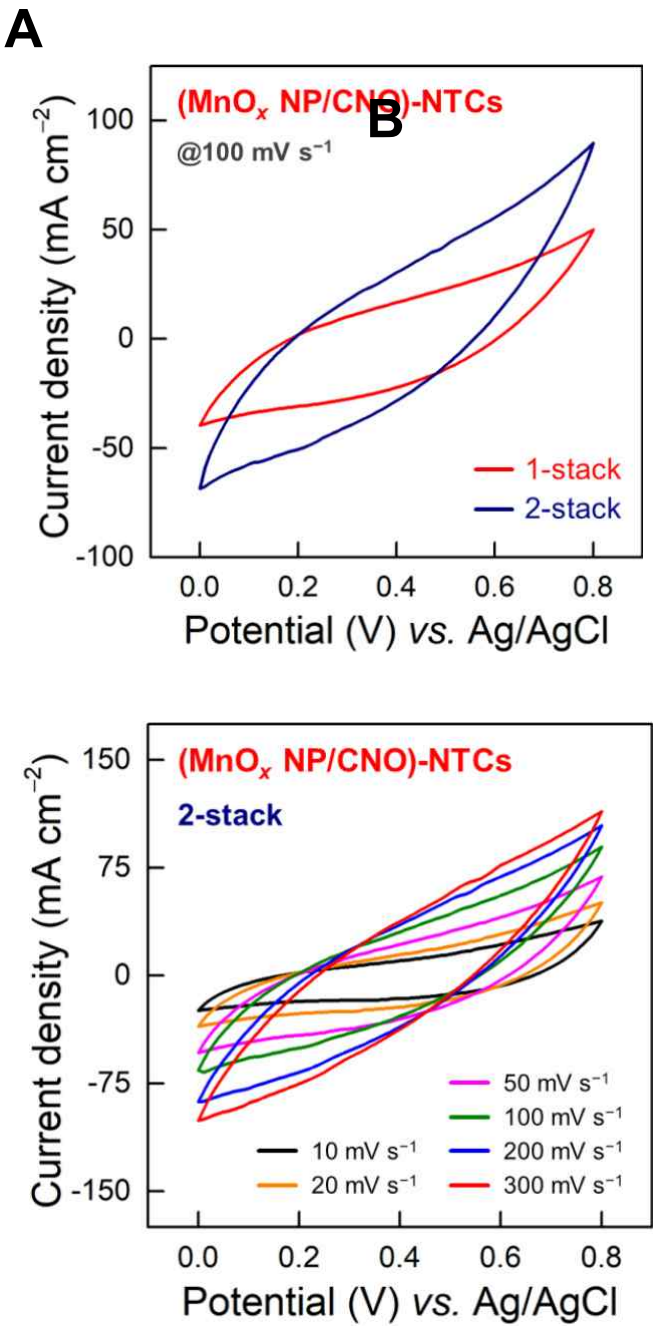

Fig. S25. (A) CV curves of non-stacked and two-stacked (MnO_x NP/CNO)-NTCs at 100 mV s^{-1}. (B) CV curves of two-stacked (MnO_x NP/CNO)-NTCs at various scan rates in the range of 10 to 300 mV s^{-1}.

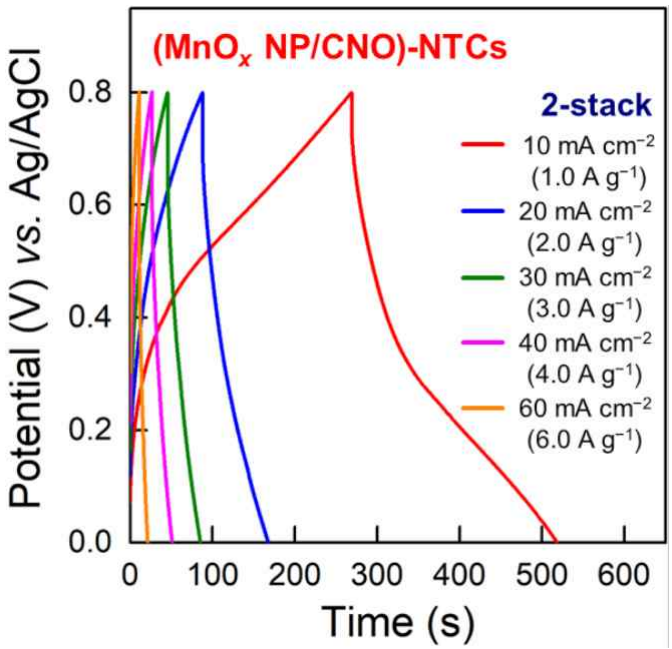

Fig. S26. GCD curves of two-stacked (MnO_x NP/CNO)-NTCs at various current densities in the range of 10 to 60 mA cm^{-2} (1.0 to 6.0 A g^{-1}).

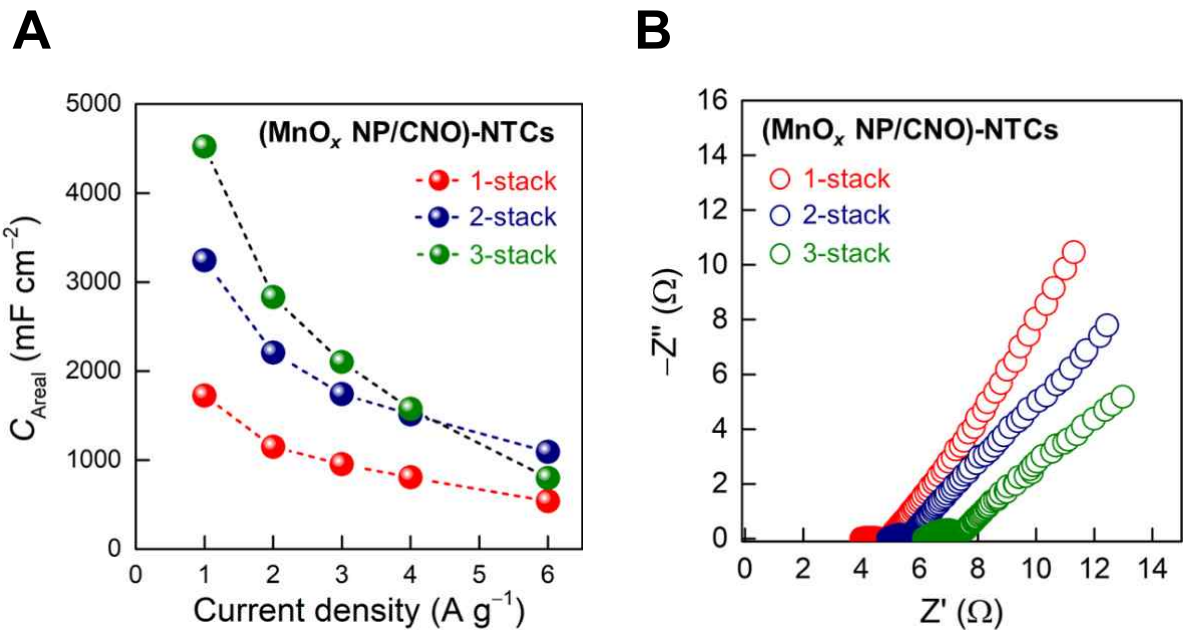

Fig. S27. (A) Areal capacitance (C_{Areal}) values of (MnO_x NP/CNO)-NTCs as a function of the multi-stacking number at different current densities in the range of 1.0 to 6.0 A g^{-1}. (B) Nyquist plots of (MnO_x NP/CNO)-NTCs as a function of the multi-stacking number.

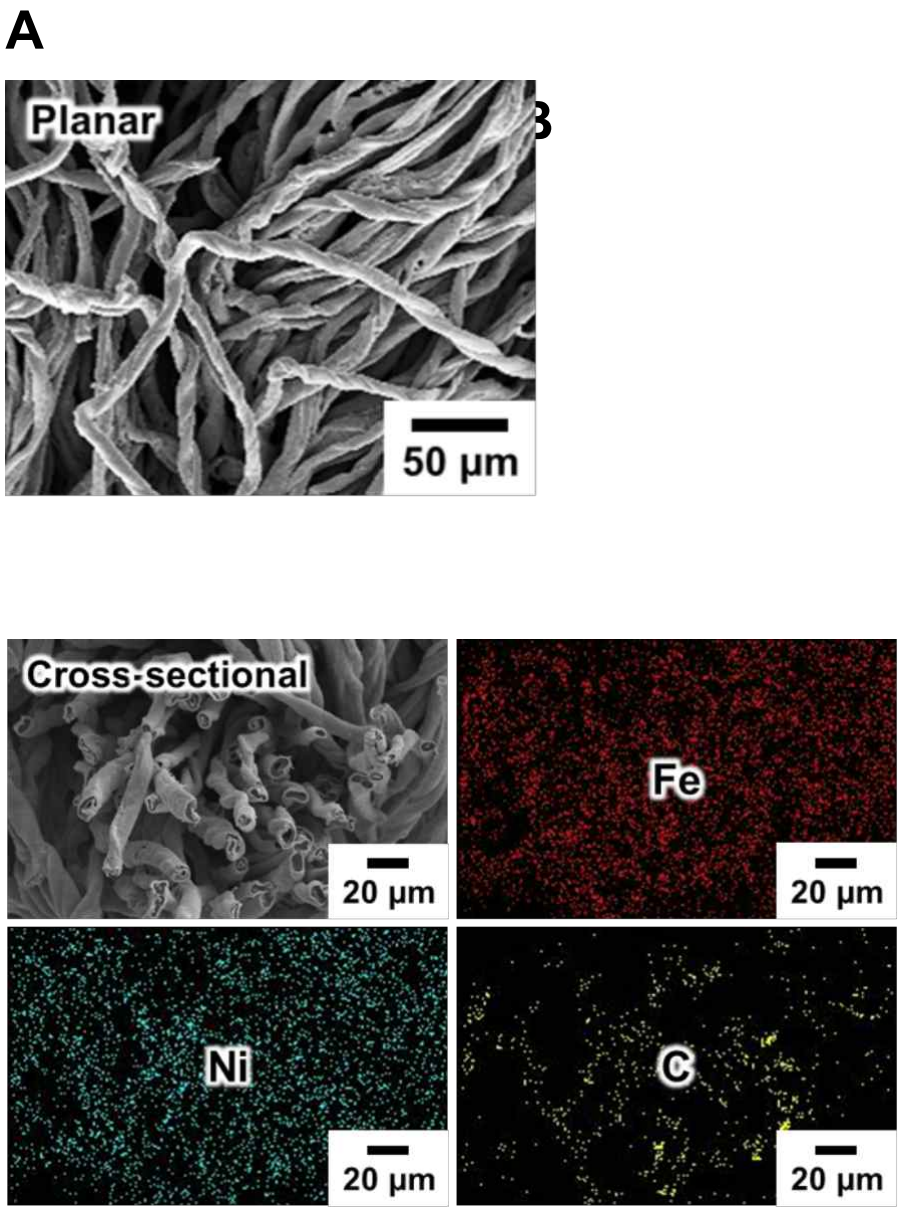

Fig. S28. (A) Planar and (B) cross-sectional FE-SEM and corresponding EDS mapping images of (Fe_3O_4 NP/CNO)-NTCs..

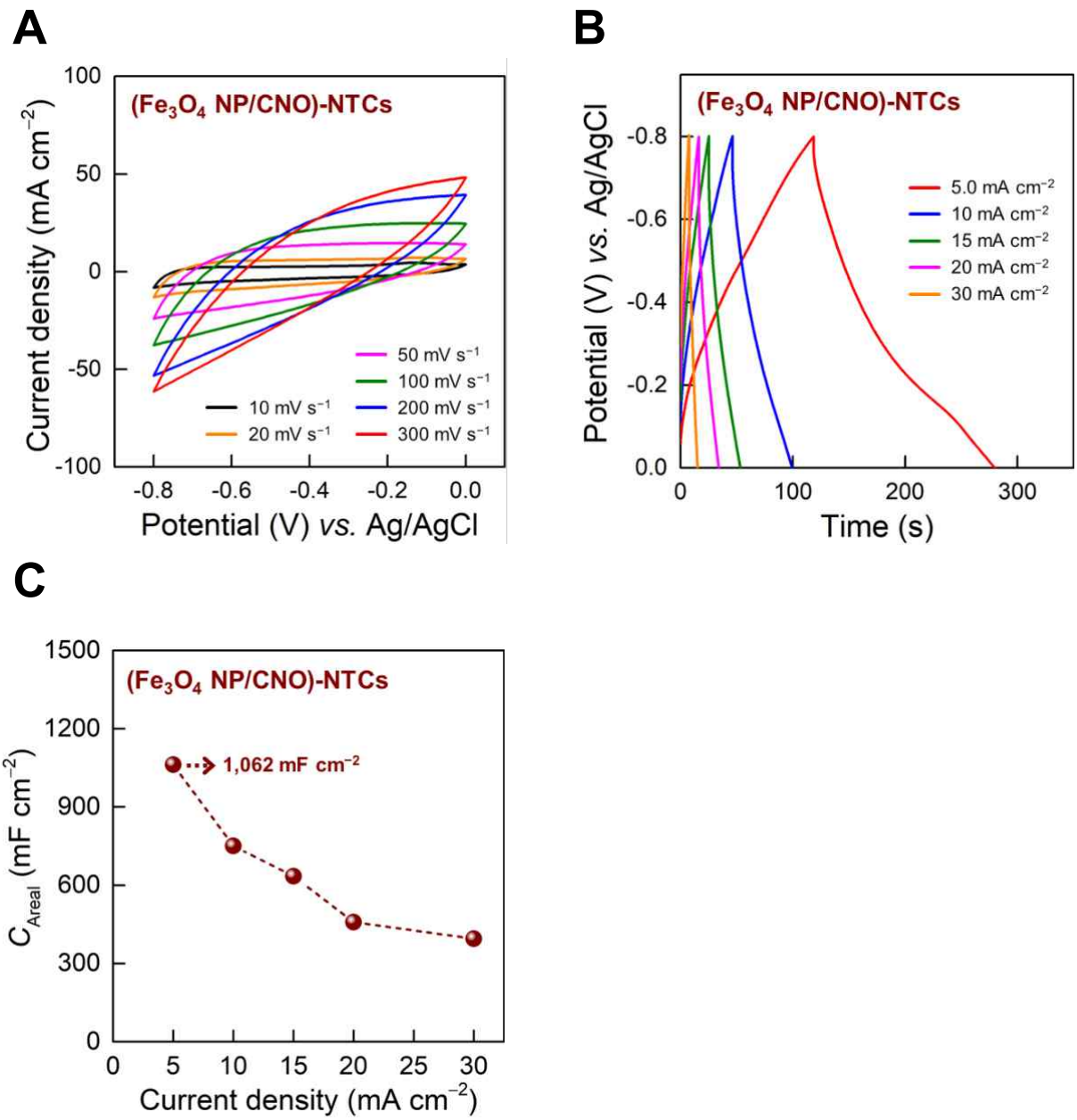

Fig. S29. (A) Scan rate-dependent CV curves, (B) current density-dependent GCD curves, and C) areal capacitance (C_{Areal}) values (at various current densities in the range of 5.0 to 30 mA cm^{-2}) of (Fe_3O_4 NP/CNO)-NTCs.

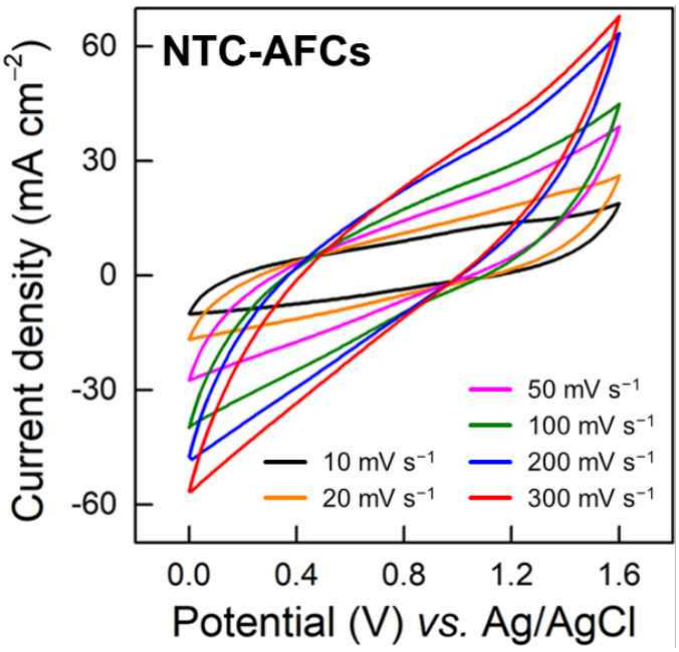

Fig. S30. CV curves of NTC-AFCs at various scan rates in the range of 10 to 300 mV s^{-1}.

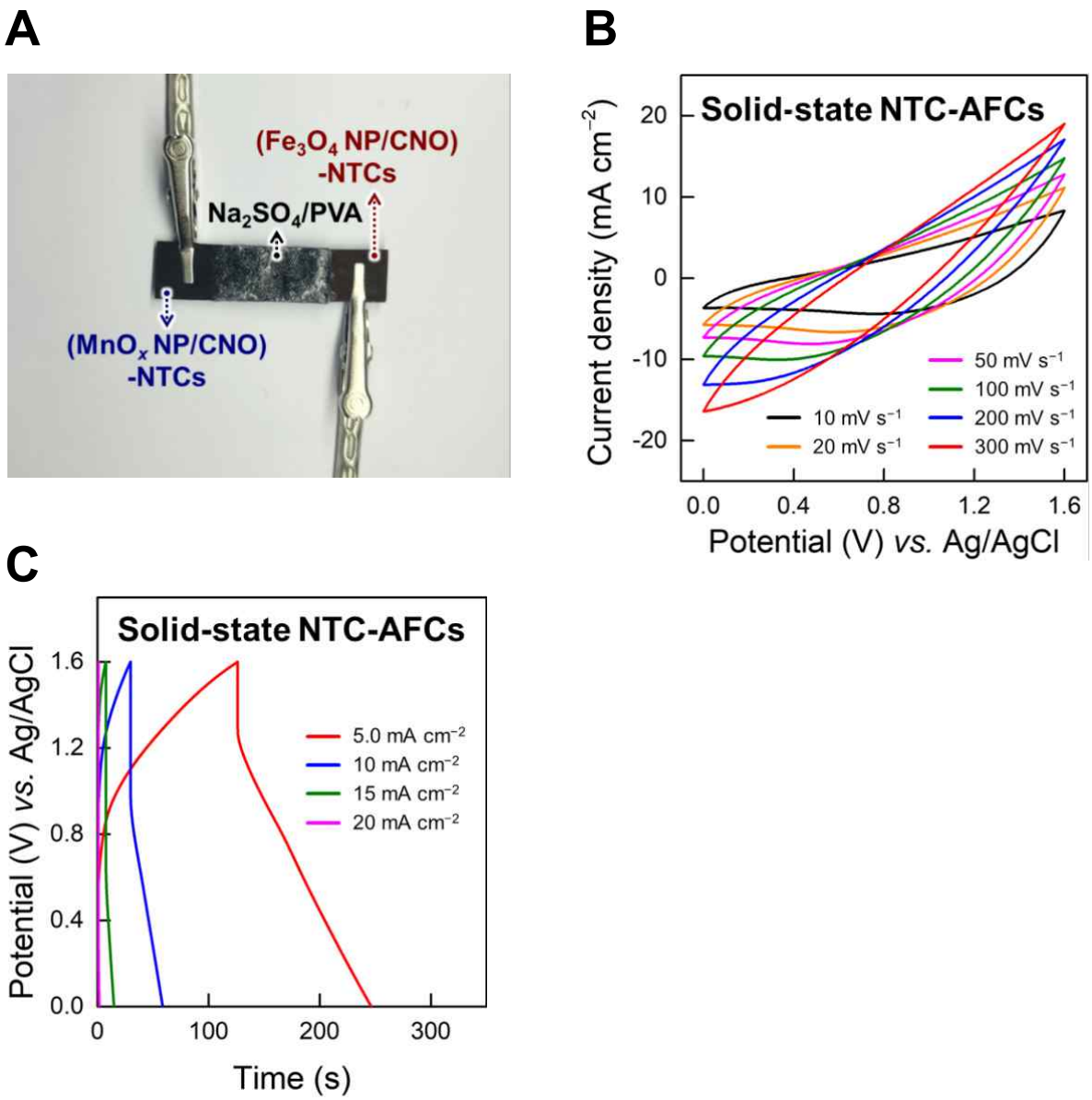

Fig. S31. (A) Digital image of solid-state NTC-AFC. (B) Scan rate-dependent CV and (C) current density-dependent GCD curves of solid-state NTC-AFCs.

Table S1. Comparison of areal capacitance values between our work and other studies using active MnO_x and 3D porous current collectors.

Electrode materials	Methods	Substrates	Electrolytes	Potential window	Areal capacitance (mF cm^{-2})	Reference
MnO_x NP/ CNO	**LbL assembly**	**NTC**	**Na_2SO_4**	**0 to 0.8 V**	**1-stack 1,725 (@1 A g^{-1}) 2-stack 3,244 (@1 A g^{-1})**	**Our Work**
MnO_2/PPy	Electrodeposition/ Polymerization	Carbon cloth	Na_2SO_4	0 to 1.0 V	1,240 (@0.3 A g^{-1})	S7
MnO_2-TEA[a)]	Slurry casting	Carbon cloth	Na_2SO_4	0 to 1.0 V	418 (@1 A g^{-1})	S8
MnO/CNF	Electrospinning/ Carbonization	Carbon nanofiber	Na_2SO_4	–0.4 to 0.8 V	533 (@0.3 A g^{-1})	S9
H-MnO_2-TEA	Slurry casting	Ni foam	Na_2SO_4	0 to 1.0 V	475 (@0.5 A g^{-1})	S10
MnO_2	Electrodeposition	Paper	Na_2SO_4	0 to 0.8 V	636 (@0.3 A g^{-1})	S11
MnO_2	Electrodeposition	Ni mesh	Na_2SO_4	0 to 0.8 V	1,150 (@0.05 A g^{-1})	S12
MnO_2/graphene	Slurry casting	Carbon cloth	Na_2SO_4	0 to 0.8 V	1,490 (@0.5 A g^{-1})	S13
Mn_3O_4/rGO	Slurry casting	Carbon cloth	Na_2SO_4	–0.1 to 1.2 V	432 (@0.7 A g^{-1})	S14
α-MnO_2/AEG[b)]	Slurry casting	Ni foam	Na_2SO_4	0 to 1.0 V	408 (@1 A g^{-1})	S15

[a)]TEA: triethanolamine; [b)]AEG: activated expanded graphite.

Table S2. Comparison of areal energy/power densities between our work and other studies using active MnO_x and 3D porous current collectors.

Positive materials (substrates)	Negative materials (substrates)	Methods	Potential window	Areal energy density (μWh cm^{-2})	Areal power density (mWh cm^{-2})	Reference
MnO_x NP/ CNO (NTC)	**Fe_3O_4 NP/ CNO (NTC)**	**LbL assembly**	**0 to 1.6 V**	**188**	**30.1**	**Our work**
MnO_2-TEA[a)] (Carbon cloth)	MoO_{3-x} (Carbon cloth)	Slurry casting	0 to 1.8 V	115	0.90	S8
H-MnO_2-TEA (Ni foam)	AC[b)] (Ni foam)	Slurry casting	0 to 2.0 V	51.6	30.0	S10
MnO_2-AC (Ni foam)	MnO_2-AC (Ni foam)	Slurry casting	0 to 1.8 V	43.2	2.20	S16
MnO/Mn_3O_4 (Carbon cloth)	AC (Carbon cloth)	Slurry casting	0 to 2.0 V	40.6	1.00	S17
Mn_2O_3/MnO_2 (Ni foam)	AC (Ni foam)	Slurry casting	0 to 1.8 V	54.0	0.20	S18
Mn_3O_4/C/rGO (Ni foam)	CNT/rGO (Ni foam)	Slurry casting	0 to 1.8 V	42.4	0.70	S19
Mn_3O_4/rGO (Carbon cloth)	VO_2/rGO (Carbon cloth)	Slurry casting	0 to 2.2 V	53.4	0.40	S14
MnO_2/GQD[c)] (Ni foam)	NG[d)] (Ni foam)	Hydrothermal	0 to 2.3 V	156	1.23	S20

[a)]TEA: triethanolamine; [b)]AC: activated carbon; [c)]GQD: graphene quantum dot; [d)]NG: nitrogen-doped graphene.

Supplementary references

[S1] J. Park, K. An, Y. Hwang, J.-G. Park, H.-J. Noh, J.-Y. Kim, J.-H. Park, N.-M. Hwang, T. Hyeon, Ultra-Large-Scale Syntheses of Monodisperse Nanocrystals, Nat. Mater. 3 (2004) 891-895. https://doi.org/10.1038/nmat1251.

[S2] S. Sun, H. Zeng, D. B. Robinson, S. Raoux, P. M. Rice, S. X. Wang, G. Li, Monodisperse MFe2O4 (M = Fe, Co, Mn) Nanoparticles, J. Am. Chem. Soc. 126 (2004) 273-279. https://doi.org/10.1021/ja0380852.

[S3] O. P. Watts, Rapid Nickel Plating, Trans. Am. Electrochem. Soc. 29 (1916) 395-403.

[S4] C.-T. Hsu, C.-C. Hu, T.-H. Wu, J.-C. Chen, M. Rajkumar, How the Electrochemical Reversibility of a Battery-Type Material Affects the Charge Balance and Performances of Asymmetric Supercapacitors, Electrochim. Acta 146 (2014) 759-768. https://doi.org/10.1016/j.electacta.2014.09.041.

[S5] Y. Song, S. Lee, Y. Ko, J. Huh, Y. Kim, B. Yeom, J. H. Moon, J. Cho, Charge-transfer effects of organic ligands on energy storage performance of oxide nanoparticle-based electrodes, Adv. Funct. Mater. 32 (2022) 2106438. https://doi.org/10.1002/adfm.202106438.

[S6] V. Augustyn, P. Simon, B. Dunn, Pseudocapacitive oxide materials for high-rate electrochemical energy storage, Energy Environ. Sci. 7 (2014) 1597-1614. https://doi.org/10.1039/C3EE44164D.

[S7] P. Zhao, N. Wang, M. Yao, H. Ren, W. Hu. Hydrothermal Electrodeposition Incorporated with CVD-Polymerisation to Tune PPy@MnO2 Interlinked Core-shell Nanowires on Carbon Fabric for Flexible Solid-State Asymmetric Supercapacitors, Chem. Eng. J. 380 (2020) 122488. https://doi.org/10.1016/j.cej.2019.122488.

[S8] A. Zhang, R. Zhao, L. Hu, R. Yang, S. Yao, S. Wang, Z. Yang, Y.-M. Yan, Adjusting the Coordination Environment of Mn Enhances Supercapacitor Performance of MnO_2, Adv. Energy Mater. 11 (2021) 2101412. https://doi.org/10.1002/aenm.202101412.

[S9] W. Xu, L. Liu, W. Weng, High-Performance Supercapacitor Based on MnO/Carbon Nanofiber Composite in Extended Potential Windows, Electrochim. Acta 370 (2021) 137713. https://doi.org/10.1016/j.electacta.2021.137713.

[S10] J. Ling, A. Gao, Y. Huang, F. Yi, Q. Li, G. Wang, Y. Liu, D. Shu, Self-Templated and Triethanolamine-Induced Hollow MnO_2 Nanoboxes with Abundant Active Mn^{3+} and Oxygen Vacancies for High-Performance Na-Ion Pseudocapacitors, Chem. Eng. J. 452 (2023) 139661. https://doi.org/10.1016/j.cej.2022.139661.

[S11] I. H. Oh, S. M. Lee, Y. W. Kim, S. Choi, I. Nam, S. T. Chang, Hydrophobic-Barrier-Assisted Formation of Vertically Layered Capacitive Electrodes within a Single Sheet of Paper, J. Mater. Chem. A 9 (2021) 27672. https://doi.org/10.1039/d1ta08854h.

[S12] Y.-H. Liu, Z.-Y. Jiang, J.-L. Xu, Self-Standing Metallic Mesh with MnO_2 Multiscale Microstructures for High-Capacity Flexible Transparent Energy Storage, ACS Appl. Mater. Interfaces 11 (2019) 24047-24056. https://doi.org/10.1021/acsami.9b05033.

[S13] C. Wang, J. Huang, Y. Huang, X. Li, W. Zhang, J. Sun, P. Xiong, Y. Fu, L. Xue, J. Zhu, Ligand Field Regulation of δ-MnO_2 by Polyanion Modification Enables Extended Potential Window in Supercapacitors, J. Power Sources 581 (2023) 233462. https://doi.org/10.1016/j.jpowsour.2023.233462.

[S14] R. Sahoo, D. T. Pham, T. H. Lee, T. H. T. Luu, J. Seok, Y. H. Lee, Redox-Driven Route for Widening Voltage Window in Asymmetric Supercapacitor, ACS Nano 12 (2018) 8494-8505. https://doi.org/10.1021/acsnano.8b04040.

[S15] P. Murovhi, D. J. Tarimo, K. O. Oyedotun, N. Manyala, High Specific Energy Asymmetric Supercapacitor Based on Alpha-manganese Dioxide/Activated Expanded Graphite Composite and Activated Carbon-Polyvinyl Alcohol, J. Energy Storage 32 (2020) 101797. https://doi.org/10.1016/j.est.2020.101797.

[S16] D. Zhang, P. Yang, Y. Zhang, H. Liu, Y. Xu, J. Wu, P. Li, Facile Synthesis of Pompon-like Manganese Dioxide Decorated Activated Carbon Composite for Supercapacitor Electrode, J. Energy Storage 56 (2022) 106134. https://doi.org/10.1016/j.est.2022.106134.

[S17] S. Wang, R. Zhao, S. Yao, X. Wang, J. Wang, X. Gao, Z. Hou, X. Liu, Z. Fu, D. Wang, J. Xie, Z. Yang, Y.-M. Yan, Spatially Expanded Built-in Electric Field via Engineering Graded Junction Enables Fast Charge Transfer in Bulk MnO@Mn_3O_4 for Na^+ Supercapacitors, Nano Energy 115 (2023) 108725. https://doi.org/10.1016/j.nanoen.2023.108725.

[S18] W. Lu, Y. Li, M. Yang, X. Jiang, Y. Zhang, Y. Xing, Construction of Hierarchical Mn_2O_3@MnO_2 Core−Shell Nanofibers for Enhanced Performance Supercapacitor Electrodes, ACS Appl. Energy Mater. 3 (2020) 8190-8197. https://doi.org/10.1021/acsaem.0c00392.

[S19] B. R. Wang, Y. Hu, Z. Pan, J. Wang, MOF-Derived Manganese Oxide/Carbon Nanocomposites with Raised Capacitance for Stable Asymmetric Supercapacitor, RSC Adv. 10 (2020) 34403-34412. https://doi.org/10.1039/D0RA05494A.

[S20] H. Jia, Y. Cai, J. Lin, H. Liang, J. Qi, J. Cao, J. Feng, W. Fei, Heterostructural Graphene Quantum Dot/MnO_2 Nanosheets toward High-Potential Window Electrodes for High-Performance Supercapacitors, Adv. Sci. 5 (2018) 1700887. https://doi.org/10.1002/advs.201700887.